The Astrophysical Journal, 932:3 (12pp), 2022 June 10 https://doi.org/10.3847/1538-4357/ac6bf5

Non-LTE Inversion of Prominence Spectroscopic Observations in Hα and Mg II h&k lines

Sonja Jejčič[1,2], Petr Heinzel[3,4], Brigitte Schmieder[5,6,7], Stanislav Gunár[3], Pierre Mein[5], Nicole Mein[5], and Guiping Ruan[8]

[1] Faculty of Education, University of Ljubljana, Kardeljeva ploščad 16, 1000 Ljubljana, Slovenia; sonja.jejcic@guest.arnes.si
[2] Faculty of Mathematics and Physics, University of Ljubljana, Jadranska 19, 1000 Ljubljana, Slovenia
[3] Astronomical Institute, The Czech Academy of Sciences, 25165 Ondřejov, Czech Republic
[4] University of Wrocław, Center of Scientific Excellence—Solar and Stellar Activity, Kopernika 11, 51-622 Wrocaw, Poland
[5] LESIA, Observatoire de Paris, Université PSL, CNRS, Sorbonne Université, Université de Paris, 5 Place Jules Janssen, Meudon, France
[6] School of Physics and Astronomy, University of Glasgow, Glasgow, UK
[7] Dept. Mathematics, Centre for mathematical Plasma Astrophysics, KU Leuven, Leuven, Belgium
[8] Shandong Provincial Key Laboratory of Optical Astronomy and Solar-Terrestrial Environment, and Institute of Space Sciences, Shandong University, Weihai 264209, People's Republic of China

Received 2021 October 27; revised 2022 April 27; accepted 2022 April 28; published 2022 June 8

Abstract

We continued our investigation of the plasma characteristics of a quiescent prominence that occurred on 2017 March 30. The prominence was observed simultaneously by several instruments, including the Interface Region Imaging Spectrograph (IRIS) and the Multichannel Subtractive Double Pass (MSDP) spectrograph operating at the Meudon solar tower. We focused on IRIS Mg II h&k and MSDP Hα spectra, selecting 55 well-coaligned points within the prominence. We computed an extensive grid of 63,000 isothermal and isobaric 1D-slab prominence models with a non-LTE (i.e., departures from the local thermodynamic equilibrium) radiative transfer code. We then performed a 1.5D spectral inversion searching for an optimal model that best fits five parameters of the observed profiles (observables), namely, the integrated intensity of the Hα and Mg II k lines, the FWHM of both lines, and the ratio of intensities of the Mg II k and Mg II h lines. The latter is sensitive to temperature. Our results show that the prominence is a low-temperature structure, mostly below 10,000 K, with some excursions to higher values (up to 18,000 K) but also rather low temperatures (around 5000 K). The microturbulent velocity is typically low, peaking around 8 km s^{-1}, and electron density values are of the order of 10^{10} cm^{-3}. The peak effective thickness is 500 km, although the values range up to 5000 km. The studied prominence is rather optically thin in the Hα line and optically thick in the Mg II h&k lines.

Unified Astronomy Thesaurus concepts: Quiescent solar prominence (1321); Radiative transfer (1335); Spectroscopy (1558)

1. Introduction

Spectra of solar prominences, and particularly quiescent ones, have been analyzed in many studies using observations from extreme ultraviolet (EUV) up to infrared—see review in Labrosse et al. (2010) and recent summaries in the book by Vial & Engvold (2015). However, only a few such analyses were carried out using the techniques of spectral inversion where the observed spectral line intensities and shapes are inverted to get the physical quantities such as kinetic temperature, density, gas pressure, spatial extension, and the velocities of macroscopic flows or oscillations. Apart from prominence thermodynamic and dynamic properties, the magnetic field was also determined by inverting spectropolarimetric data—see the review by López Ariste (2015) and other related papers, such as Merenda et al. (2006), Martínez González et al. (2015), Martínez González et al. (2016), and Wang et al. (2020) where observations of helium lines were used. All the above parameters can be obtained only by analyzing the prominence radiation, and namely, high-resolution and high-dispersion spectra. Their precise knowledge is key for our understanding of the thermodynamic and dynamic structure of the prominence plasma embedded in the magnetic field. For example, the kinetic temperature constrains various models of the prominence heating/cooling, see, e.g., the discussion of the radiative equilibrium in Heinzel et al. (2014) and a general review of prominence energy balance by Gilbert (2015). Another example is the prominence magnetic topology inferred both from extrapolations and from spectropolarimetric inversions (Mackay et al. 2020). All of this information is crucial to our understanding of the formation and instability of prominences, their mass loading, and their dynamics that can lead to coronal mass ejections (CMEs). Similar inversion techniques are now widely used also in the case of the solar chromosphere where high-resolution spectral observations, e.g., from the Swedish Solar Telescope (SST) or the Interface Region Imaging Spectrograph (IRIS; De Pontieu et al. 2014) allow deriving the height variation of the above-mentioned plasma parameters. Namely, the new STockholm inversion Code (STiC) is capable of inverting the data from various instruments (e.g., Sainz Dalda et al. 2019; da Silva Santos et al. 2020). The method of extensive model grids similar to that used in this paper was successfully applied to photospheric (Riethmüller et al. 2017) and chromospheric observations (Beck et al. 2019). In the case of prominences or filaments (i.e., prominences seen in projection against the solar disk) see Molowny-Horas et al. (1999) and Tziotziou et al. (2001) who analyzed Multichannel Subtractive Double Pass (MSDP; Mein 1977, 1991; Mein & Mein 1991) observations of quiescent filaments taken in the hydrogen Hα line

or in the Ca II 8542 Å infrared line, respectively. Contrary to the STiC inversion method, these authors produced a database of synthetic profiles computed from a large grid of 1D-slab non-LTE (i.e., departures from the local thermodynamic equilibrium) filament models, covering a range of slab temperatures, gas pressures, effective geometrical thicknesses, and microturbulent velocities. Such a data set was then used to search for the best-fit model by minimizing the corresponding merit functions. Quite recently, Peat et al. (2021) inverted Mg II h&k line profiles in an off-limb prominence observed by IRIS using the 1D models of Levens & Labrosse (2019). A similar approach was also applied by Barczynski et al. (2021) to spectra of this tornado-like prominence, but a good fitting was achieved only in areas of low optical thickness of the prominence, mainly in its top and edge parts. For the core of a CME (erupting flux rope), a similar inversion of hydrogen Lyα and Lyβ lines detected by the Ultra-Violet Coronagraph Spectrometer on board the Solar and Heliospheric Observatory was performed by Heinzel et al. (2016), while in the case of a loop prominence (flare loops) such a technique was recently applied in Koza et al. (2019) who inverted Hβ and Ca II 8542 Å spectral line profiles obtained with SST. Ruan et al. (2019) applied an inversion based on a large grid of non-LTE models, but these authors inverted only the characteristic parameters of the Hα line observed by MSDP (integrated line intensity and the FWHM). Since the observed emission-line profiles of Hα were rather broad in many positions within the prominence, the inversion of Hα alone led to a large scatter in the distribution of plasma temperatures and micro-turbulent velocities (kind of bifurcation). Here we have to note that all these inversions of prominence/filament spectra used precomputed synthetic line intensities in absolute radiometric units. This is very important because fitting only the line shapes (e.g., profiles normalized to the central intensity) may lead to spurious results.

In the present paper, we fully exploit simultaneous prominence observations in the Hα and Mg II h&k lines, as presented in Ruan et al. (2019). Intuitively it is clear that adding the Mg II lines to inversion should improve the solution significantly because (i) Mg II lines are very sensitive to nonthermal broadening (microturbulence), and (ii) as shown in Jejčič et al. (2018) the ratio of integrated intensities of two Mg II lines varies with the temperature. Therefore, we increase the number of observables in our inversion procedure. However, as in Ruan et al. (2019), we fit only these specific line characteristics rather than full line profiles. The reason for this is explained below.

The paper is organized as follows. In Section 2, we briefly describe the observations and how we define various observables. In Section 3, we present the grid of prominence models and the inversion strategy. Section 4 then presents various results and Section 5 presents the discussion. Section 6 presents our conclusions.

2. Prominence Observations

A quiescent prominence on the northwestern limb was observed with multiple instruments in space and on the ground on 2017 March 30. We focus on the simultaneous ground-based data obtained with the MSDP spectrograph at the Meudon solar tower, and on the high-resolution space data obtained by IRIS. MSDP produces Hα spectra at 6563 Å in a 2D field of view (FOV), while for IRIS we used Mg II h&k spectroscopic data at 2803.5 Å and 2796.4 Å together with slit-jaw (SJ) images at 2796 Å. The MSDP FOV is $450' \times 230'$ with a pixel size of $0\farcs5$, while for IRIS the 32 positions of the slit cover a range of $64' \times 120'$ with a step of $2'$ between two slit positions with a spatial sampling of $0\farcs33$ per pixel along the slit. The FOV of IRIS SJ images is $167' \times 175'$. MSDP observations were made between 07:25:54 and 08:55:28 UT, while IRIS was observing between 07:06 and 08:46 UT. Details of these observations can be found in Ruan et al. (2018, hereafter Paper I) and in Ruan et al. (2019, hereafter Paper II).

Coalignment between simultaneously observed MSDP maps and IRIS SJ images was performed, as can be seen in the left and in the middle panels of Figure 1. In total, we obtained 75 coaligned observational points (pixels) within the studied prominence, but we discarded those that have very asymmetrical profiles or are too close to the solar disk. In this way, we obtained in total 55 points marked in the right panel of Figure 1.

The MSDP spectrograph yields Hα profiles with a spectral sampling of 0.30 Å. As shown in the left panel of Figure 2, finer spectral sampling is obtained by polynomial interpolation. To increase the wavelength range to ± 0.7 Å, we extrapolated the wings of the Hα profiles using a Gaussian fit and integrated entire profiles to calculate the integrated intensities of Hα. The σ parameter of the Gaussian fit specifies the FWHM. Both parameters play an important role in a spectral inversion. The right panel in Figure 2 shows an example of a reversed and asymmetrical Mg II k profile due to the motions of the prominence fine-structure elements, which is the prevalent shape within the prominence. Integrated intensities of the Mg II lines are calculated for the whole wavelength range. Because of the shape of Mg II profiles, we decided to define the FWHM as based on the central intensity, i.e., the intensity of the line peak in the case of the Hα line and the minimum intensity of the central reversal in the case of Mg II h&k lines. The same approach was later applied to synthetic profiles. Note that the synthetic spectra were convolved with the instrumental profile of the MSDP spectrograph, which has an FWHM of 0.18 Å (Paper II), and the instrumental profile of the IRIS spectrograph, which has an FWHM of 52 mÅ (Heinzel et al. 2014), to simulate observed profiles.

3. Inversion Approach

3.1. Grid of Non-LTE Models

To facilitate the inversion of the observed line profiles, we have computed an extensive grid of 1D-slab prominence models in non-LTE. The Multilevel Accelerated Lambda Iteration (MALI) code used for that is described in Heinzel et al. (2014). A 1D slab with finite effective thickness $D_{\rm eff}$ stands perpendicularly above the solar surface and is illuminated by radiation from the solar disk. We use a five-level plus continuum model atom for both hydrogen and magnesium. At typical prominence temperatures the model Mg II–Mg III is a reasonable one (see also Peat et al. 2021), but see the discussion below. To characterize the main cool body of the prominence we use simple isothermal-isobaric models and neglect the prominence-to-corona transition region (PCTR); we also discuss this later. We use partial frequency redistribution (PRD) for hydrogen Lyα and Lyβ, which affects the computed electron density and the Hα line intensity. We also use the PRD for Mg II h&k resonance lines, but as demonstrated in Heinzel et al. (2014) this affects only the line wings, which are typically

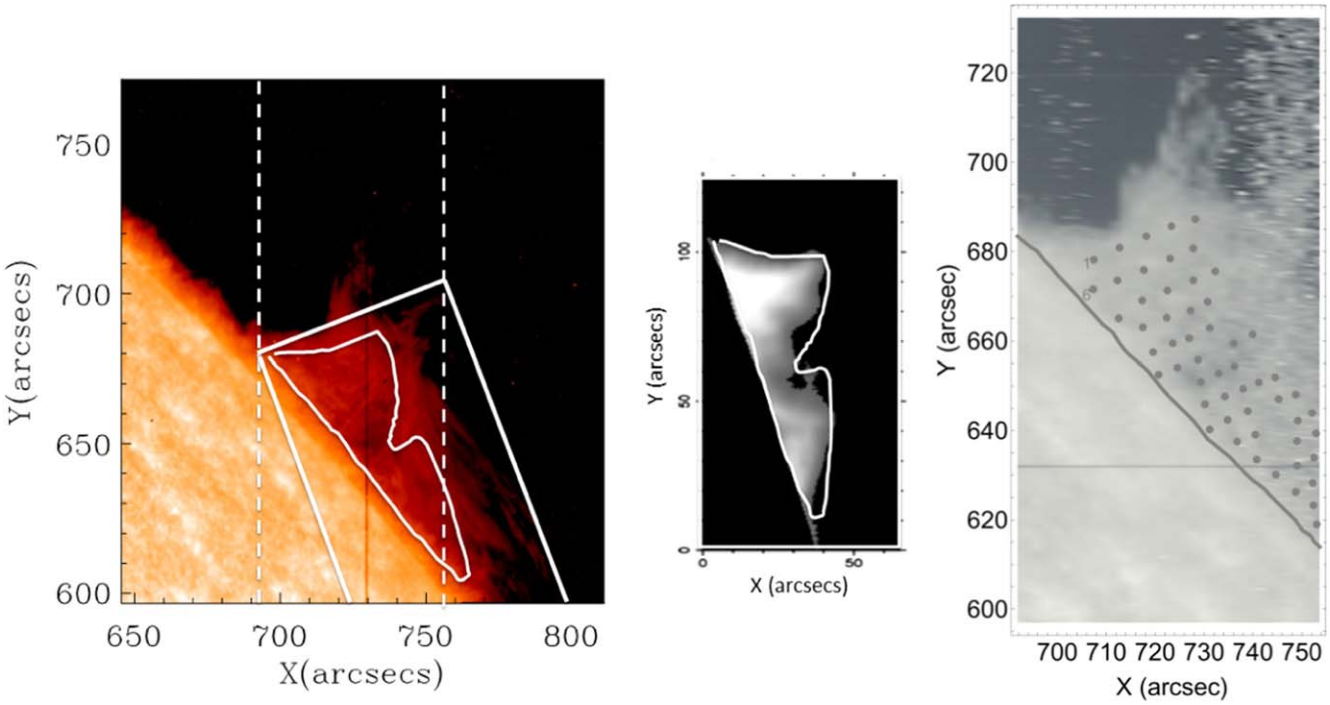

Figure 1. An example of IRIS SJ image at 2796 Å in the background, well coaligned with the MSDP contour in the foreground (white outline). The red vertical line represents the slit position of IRIS during the observations and the white dashed lines are the boundaries of the IRIS rasters (left panel). An example of an MSDP prominence together with a white MSDP contour (middle panel). The MSDP white box has a size of $80' \times 120'$. In the right panel all 55 coaligned observational points within the prominence are marked. The two numbers 1 and 6 in the diagram indicate the order of the selected observational points. The solar limb is indicated by the solid line. The silhouette of the solar disk and prominence can be seen in the background of the IRIS 2796 SJ image.

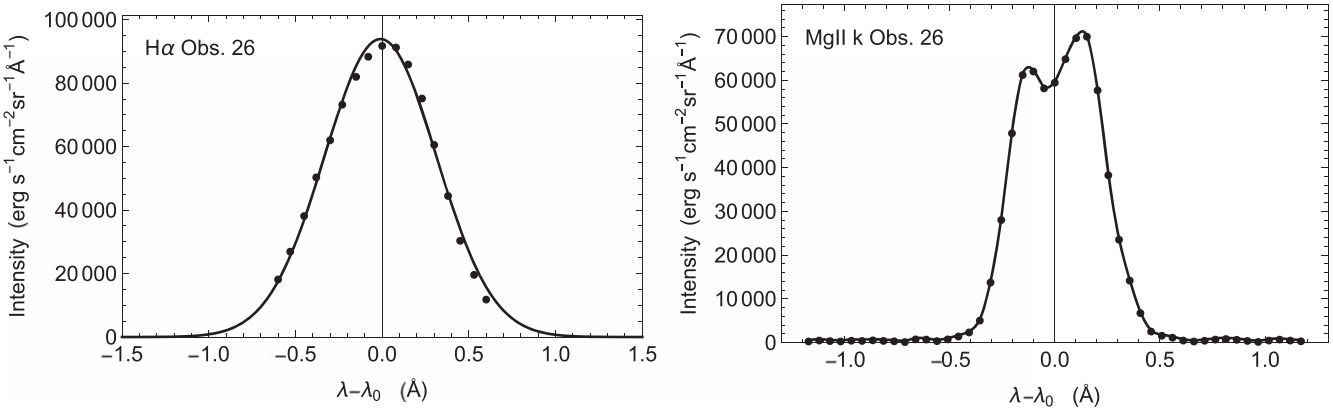

Figure 2. Left panel: a typical Hα profile that resembles a Gaussian profile with a limited MSDP wavelength range. Observations are indicated by points and the best Gaussian fit by the curve. Right panel: example of a slightly asymmetrical Mg II k profile. Most of these profiles show a central reversal and are usually asymmetrical.

much weaker than the line cores. We run the MALI code in four nested loops, varying the basic input parameters of the 1D slab: kinetic temperature T, gas pressure p, effective geometrical thickness $D_{\rm eff}$ (this is the thickness for which the line-of-sight filling factor is 1), and the microturbulent velocity $v_{\rm t}$. The height above the solar surface H is set to an average value of 13,000 km. This height determines the geometrical dilution factor for the illumination of the prominence slab by the incident disk radiation.

As the output, we get the hydrogen and Mg II ionization, the central optical thickness τ of all lines and the line profile intensities. In Table 1 we summarize the range of the input

Table 1
List of Input Parameters Used in the 1D non-LTE MALI Code

Input Parameters	Values	Step
T (kK)	4–21	0.5
p (dyn cm^{-2})	0.01–0.5	log step[a]
$D_{\rm eff}$ (km)	500–5000	500
$v_{\rm t}$ (km s^{-1})	4–22	2
$v_{\rm rad}$ (km s^{-1})	0	…
H (km)	13,000	…

Note. All combinations together lead to a total number of 63,000 models.
[a] For the gas pressure we use a logarithmic step with 9 points per decade. In total, we obtain 18 different values for a given range of selected gas pressures.

parameters, together with the steps between models. All together we computed 63,000 models.

3.1.1. Incident Radiation

The incident radiation is one of the key input parameters of the radiative transfer models. As such, it can strongly influence the synthetic profiles produced by the models. Moreover, the radiation from the solar disk in the Lyman (Gunár et al. 2020) and Mg II h&k (Koza et al. 2022) lines changes significantly during the solar cycle. As was shown by Gunár et al. (2020), the change in the intensity of the incident radiation in Lyman lines strongly affects not only the intensities of the synthetic Lyman lines but also the Hα line. The synthetic Mg II h&k profiles are also very sensitive to the change of the incident radiation—see Gunár et al. (2022). Due to this strong sensitivity, here we used incident radiation data, which closely correspond to the situation during the time when the studied prominence was observed. For the Lyman lines, we used the Lyα reference profile from Gunár et al. (2020) and the reference profiles of higher Lyman lines from Warren et al. (1998) adapted by a specific coefficient to the data of observations. We derived this coefficient from a 7 day average of the LISIRD composite Lyα index (Machol et al. 2019) centered on 2017 March 23. This date is used because regular solar disk observations are obtained only from the direction of Earth. To use observations of the exact situation on the solar disk visible from the perspective of the studied prominence, we would need full-disk observations from the direction perpendicular to the Sun–Earth line. Such observations, however, do not exist. In their absence, we used the data obtained 1 week before the prominence was observed on the west limb. While not exact, this approach allows us to obtain the best estimate of the conditions on the solar disk on the date of the prominence observations (2017 March 30). For the Mg II h&k incident radiation, we used the disk-averaged reference profiles from Gunár et al. (2021) adapted by coefficients derived using the method of Koza et al. (2022). To do so, we used the 7 day average of the Bremen Mg II index (Snow et al. 2014) centered on 2017 March 23. The incident radiation used here is diluted depending on the height of the prominence.

We consider the same dilution for all prominence pixels and compute it for an averaged height of 13,000 km. By using the average height, we get about 10% uncertainty in the dilution factor between this height and pixels close to the limb or close to prominence top. This is quite small compared to the uncertainties stemming from the use of 1D models. Computing the entire model grid for each pixel height would greatly increase the size of our model database.

3.2. Spectral Line Inversion of Hα and Mg II Lines

Contrary to some of the studies mentioned in the Introduction, here we do not invert the whole line profiles but rather their key characteristics (parameters or observables) that are sensitive to plasma conditions in the central (cool) parts of the prominence. Performing spectral line inversions, we look for the minimum of the merit function, i.e., the weighted sum of the squared differences (residuals) between the observed and synthetic data. This data is represented by a set of N parameters that characterize the spectral line profiles. The merit function, weighted by the product of the uncertainty of observations and observed data, is then defined as

$$\mathcal{L}(\boldsymbol{p}) = \frac{1}{N}\sum_{i}^{N}\left[\frac{\mathrm{obs}_i - \mathrm{syn}_i(\boldsymbol{p})}{\sigma_i\ \mathrm{obs}_i}\right]^2. \quad (1)$$

Here p is the set of prominence physical quantities that are to be inferred by the inversion. The abbreviation obs stands for observed data and syn for synthetic data (synthetic observables). The inversion is done pixel by pixel. We assume that σ is equal to 0.3 for all Hα parameters and 0.2 for all Mg II parameters. In this way, a good fit is obtained when $\mathcal{L} \sim 1$, which means that the difference between the data and synthetic parameters is of the order of the uncertainty in observations. We use this rather heuristic approach because it is difficult to quantify the actual uncertainty of different observables. However, we found that our results depend only weakly on the values of σ.

We use a merit function with five different spectral parameters for all 55 observational points within the prominence structure and an extended grid of 63,000 synthetic 1D-slab prominence models. Since we compare observational points in the 2D map pixel by pixel with 1D non-LTE models, we call this a 1.5D spectral inversion. Our five observables are representative of the Hα and two Mg II line profiles: the integrated intensities emitted in the Hα line (E_α) and the Mg II k line (E_k), the FWHM of the Hα line (FWHM$_\alpha$) and of the Mg II k line (FWHM$_\mathrm{k}$), and the ratio between the energy emitted in the Mg II k and Mg II h lines ($E_\mathrm{k}/E_\mathrm{h}$). The latter observable is used here to include also the Mg II h line and because the ratio of the emission in the two Mg II lines is temperature sensitive as previously shown in Ječič et al. (2018). Note that we compare the spectral line parameters rather than the whole profiles of all three lines because we use a simple 1D code that neglects the dynamics of the prominence elements—here a dynamical line broadening is accounted for schematically by increasing the microturbulent velocity but this does not produce the peak asymmetry often detected in Mg II lines (see the discussion in Section 5). The 1.5D inversion with the Hα line and both Mg II lines is performed for each observational point within the prominence, and as a result, we select the model with $\mathcal{L}$ closest to one due to uncertainties of the observations. In this way, we are able to derive physical quantities such as the kinetic temperature, gas pressure, effective thickness, microturbulent velocity, electron density n_e, and also the optical properties in each pixel. Figure 3 shows several examples of the best agreement between observed profiles and the synthetic ones for the Hα and Mg II lines. The differences in amplitude and width are up to 20% for the Hα line and up to 35% for both Mg II lines. Note that we compare the observations with static synthetic models, which additionally contributes to these differences.

At this point we would like to comment on our inversion strategy for prominences. We are able to precompute very extensive grids of sophisticated non-LTE prominence models because our 1D-slab models are specified by only a few parameters. Once we have such a grid, we can invert the spectra of the entire 2D FOV in a relatively short time. On the other hand, classical inversions where one proceeds step by step to a minimum of the merit function required, for each pixel, tens or hundreds model calculations that have to be repeated again for other observations. However, precomputing large grids is not only computationally advantageous, but these grids have another key property: when we search through them

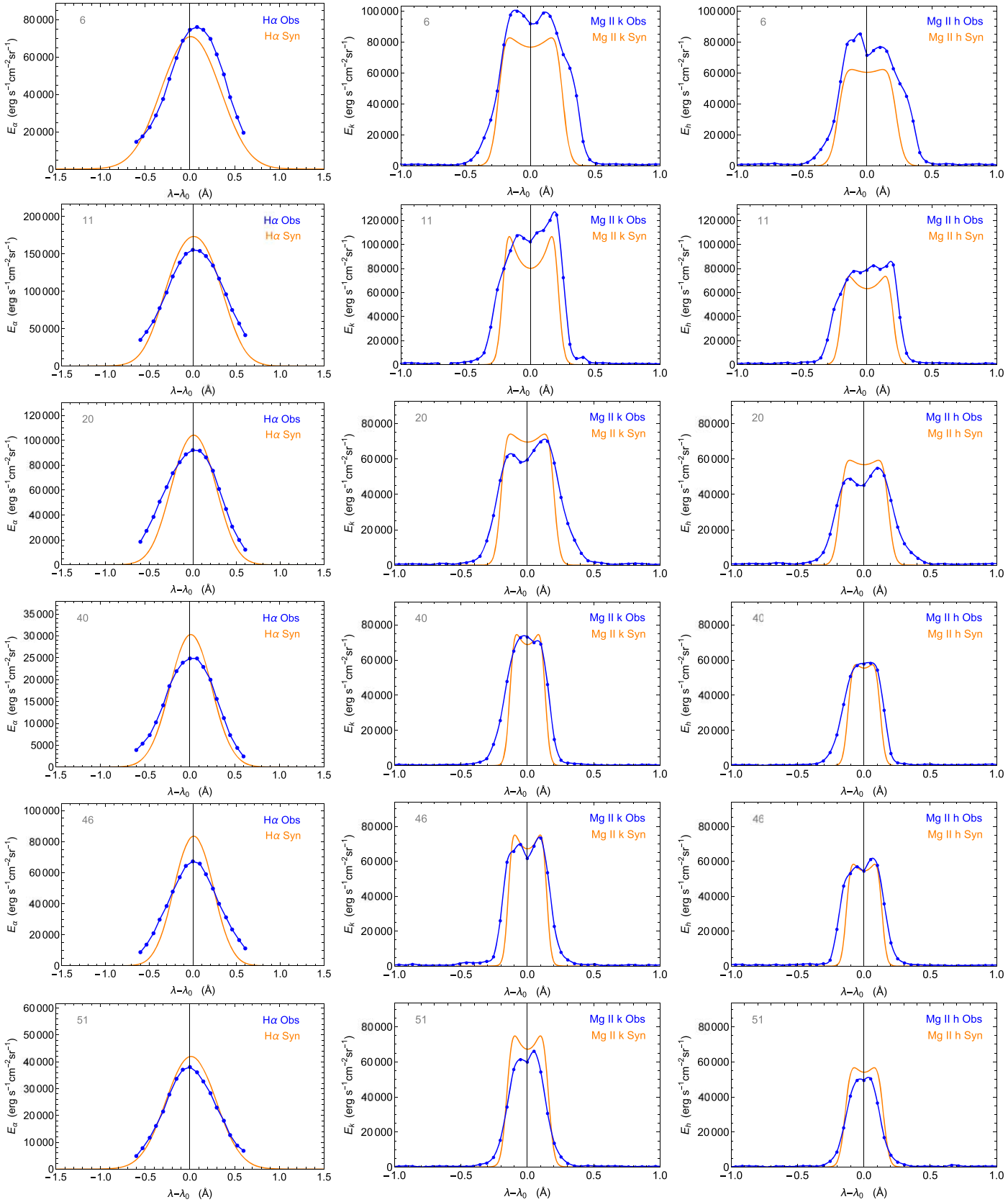

Figure 3. Comparison between observed (in blue) and best-fit synthetic profiles (in orange) for the Hα line (left column), the Mg II k line (middle column), and the Mg II h line (right column). The six profiles are from regions with temperatures between 4500 and 10,000 K, of which four points lie near the solar limb and two (40 and 51) are at more distant locations.

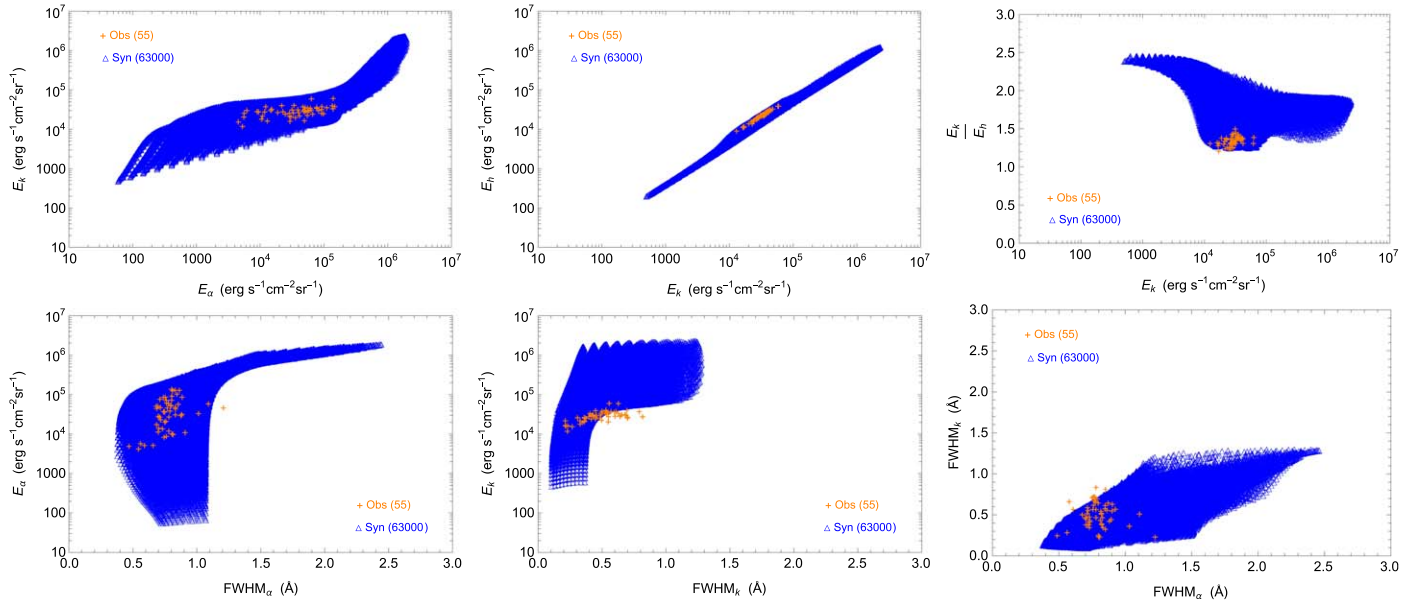

Figure 4. The relationships between the parameters used in the merit function $\mathcal{L}$ are shown for the observation data (in orange) and all synthetic models (in blue). The upper row shows the comparison between the integrated intensity emitted in the Mg II k and Hα lines, between both Mg lines, and between the ratio between both Mg lines and the Mg II k line. The lower row shows a comparison between the integrated intensity and the FWHM for the Hα and Mg II k lines, and between the FWHM of the Hα and Mg II k lines.

for the best fit, we always find the global minimum because the grid practically maps the whole multidimensional space of parameters. On the contrary, the classical methods may find only a local minimum. There are other more sophisticated techniques based, e.g., on Monte Carlo mapping of the whole space, which are capable of finding the global minimum, but they require even much more runs of the non-LTE code. We plan to test the latter methods using parallel computing machines.

4. Results of Inversion

Our results of the 1.5D spectral inversion with five spectral parameters for the Hα line and both Mg II lines, in all 55 observed points within the studied quiescent prominence, are presented as scatter plots and 2D maps, which have been produced as contour plots.

Figure 4 shows that the large grid of non-LTE models highlighted in blue practically covers the range of observations highlighted in orange for almost all parameters used in a merit function $\mathcal{L}$. The only exception is the lower middle row, which shows that some observations are slightly outside the grid.

The left upper panel of Figure 5 shows a scatter plot between the microturbulent velocity and kinetic temperature for all 55 observed points. The results show that the spectral inversion with the Hα line and both Mg II lines, favors solutions with lower kinetic temperatures. The majority of the points have temperatures lower than 10,000 K, which is typical in quiescent prominences. However, about half of the points have a relatively low temperature below 6000 K. Models for low temperatures are discussed in Section 5. The majority of the points have a low microturbulent velocity with a peak around 8 km s^{-1} and about one-third of the points have a microturbulent velocity of more than 10 km s^{-1}. The correlation coefficient between these two values is low, as shown in Table 2. In the grid of models the temperature and microturbulent velocity are two independent input parameters and thus in Table 2 we cannot indicate any theoretical correlation. However, for given observed spectral line widths certain anticorrelation is naturally expected. The middle upper panel shows the scatter plot between the integrated intensity emitted in the Mg II k line and the microturbulent velocity for the observations and the best-fit synthetic data. The values are highly correlated, as shown in Table 2. The upper right panel shows the energy emitted in the Mg II k line and the Hα line for the observations and the best-fit synthetic data. The values show a weak correlation of about 0.5 as shown in Table 2. The lower left panel shows a correlation between the integrated intensity emitted in both Mg II lines. The correlations between the observations and the best-fit synthetic data are very high (see Table 2) because the code accounts for the incident radiation of hydrogen and Mg II lines at the actual time of observations. The middle and right lower panels show scatter plots of the ratio between the two Mg II lines as a function of the energy emitted in the Mg II k line or as a function of temperature, respectively. Temperature variation is somewhat hidden in the cloud of points, but there is diagnostically relevant dependence as shown in Jejčič et al. (2018), see Figure 19 therein. The correlation coefficients for the last two plots are weak (Table 2). Note that this simple 1D modeling assumes symmetric profiles, which means that the only dynamical broadening is represented by the microturbulent velocity.

The integrated intensity emitted in the Hα line versus optical thickness is shown in the upper left panel of Figure 6 for all synthetic models highlighted in blue and all observations highlighted in orange to show that the observations lie within the large grid of models. The upper right panel shows the same plot for the observations and the best-fit synthetic data. The values are highly correlated, as can be seen in Table 2. The same plots are shown in the lower panels for the Mg II k line. Here the values show no correlation between the integrated intensity emitted in the Mg II k line and its optical thickness.

The left panel of Figure 7 shows the intensity map of the studied prominence together with the solar limb. In the middle panel, we see a 2D map of the kinetic temperature in the

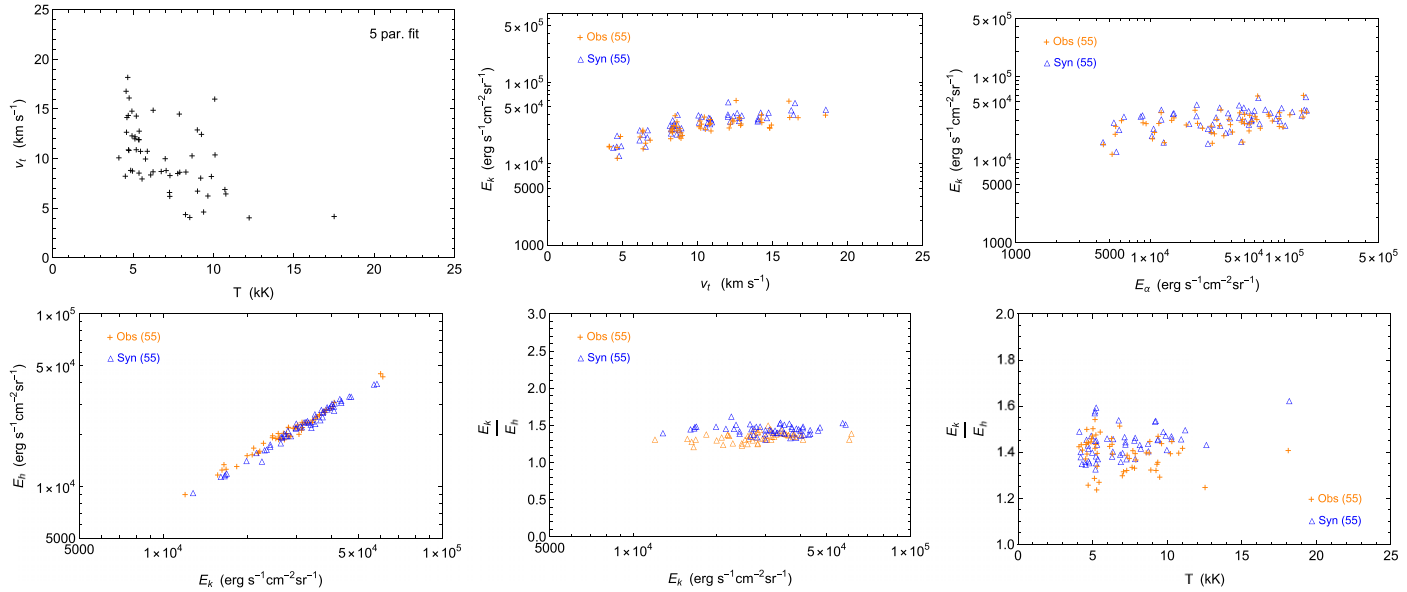

Figure 5. Upper row from left to right: microturbulent velocity vs. kinetic temperature for all 55 observed points within the studied prominence. Note that for better visualization, points with the same kinetic temperature or microturbulent velocity are randomly changed by a small amount. The same is true for other scatter plots. Integrated intensity of the Mg II k line vs. microturbulent velocity for the observations and the best-fit synthetic models, and the energy emitted in the Mg II k line vs. the Hα line in the observational domain. The lower row from left to right shows the observational domain for the relation between the integrated intensities of the two Mg II lines, the ratio between the two Mg II lines vs. the integrated intensity emitted in the Mg II k line, and finally the ratio between the two Mg II lines vs. the kinetic temperature. The correlation coefficients for all observed and best-fit data are shown in Table 2.

Table 2
Correlation Coefficients between the Various Parameters for 55 Selected Points within the Prominence as Plotted in Figures 5 and 6

	$\frac{v_t}{T}$	$\frac{E_k}{E_\alpha}$	$\frac{E_k}{v_t}$	$\frac{E_h}{E_k}$	$\frac{\frac{E_k}{E_h}}{E_k}$	$\frac{\frac{E_k}{E_h}}{T}$	$\frac{E_\alpha}{\tau_\alpha}$	$\frac{E_k}{\tau_k}$
Observations	−0.535	0.515	0.724	0.991	0.331	−0.232	0.954	0.144
Synthetic models		0.456	0.843	0.989	−0.202	0.548	0.953	0.064

studied prominence. Only a small central part reaches temperatures above 10,000 K; the rest of the prominence is a low-temperature structure with temperatures of about 5000 K. The right panel shows the 2D map of the microturbulent velocity. The left-side edge of the prominence has a microturbulent velocity higher than 10 km s^{-1}, while a narrow central belt has a microturbulent velocity lower than 6 km s^{-1}.

The upper left panel of Figure 8 shows a 2D map of the electron density, which is proportional to the gas pressure, as shown in the upper middle panel. Here we see that the electron density is on the order of 10^{10} cm^{-3}, which is a typical value for quiescent prominences. Both boundaries of the studied prominence have somewhat higher values. The upper right panel shows that the effective thickness has no particular pattern. All values are randomly distributed over the entire prominence, which may be related to the high porosity of the prominence. The lower panels show the optical thicknesses of all three lines. The Hα line is mainly optically thin, except for the lower left part, which reaches values above 0.5. In the two Mg II lines the prominence is optically thick.

In order to demonstrate the effectiveness of our approach, we plot in Figure 9, similarly as in Molowny-Horas et al. (1999), Tziotziou et al. (2001), or Koza et al. (2019), 2D distributions of the merit function in selected 2D cuts of the parameter space (for a given observed point). The shape of the $\mathcal{L}$ surface demonstrates that a single unique best-fit solution is found. For the case of the relation between temperature and microturbulent velocity, the use of lines Hα and Mg II h&k from two different species seems to help breaking the ambiguity between temperature and nonthermal velocities.

The error of the inversion method was estimated by changing five observables used in the merit function by 10% for a given pixel. As a result, the temperature changes by 4%, the gas pressure by 11%, the effective thickness by 65%, the electron density by 7%, and the microturbulent velocity by 12%.

5. Discussion

As can be seen in the left upper panel of Figure 5, several prominence pixels have a kinetic temperature below or around 5000 K, which deserves certain discussion. In principle, such temperatures are possible if the prominence structure reaches radiative equilibrium (RE), which means that the radiative cooling and radiative heating of the plasma are in exact balance. Such models have been considered in the past by, e.g., Heasley & Mihalas (1976) and recently by Gouttebroze (2007), Heinzel & Anzer (2012), and Heinzel et al. (2014). In the latter paper, the authors included hydrogen, Ca II, and Mg II net radiative losses and showed that at higher gas pressures and for larger thicknesses the central temperature can indeed drop down below 5000 K under the RE conditions. It is interesting to note that the relaxation times needed to reach such an

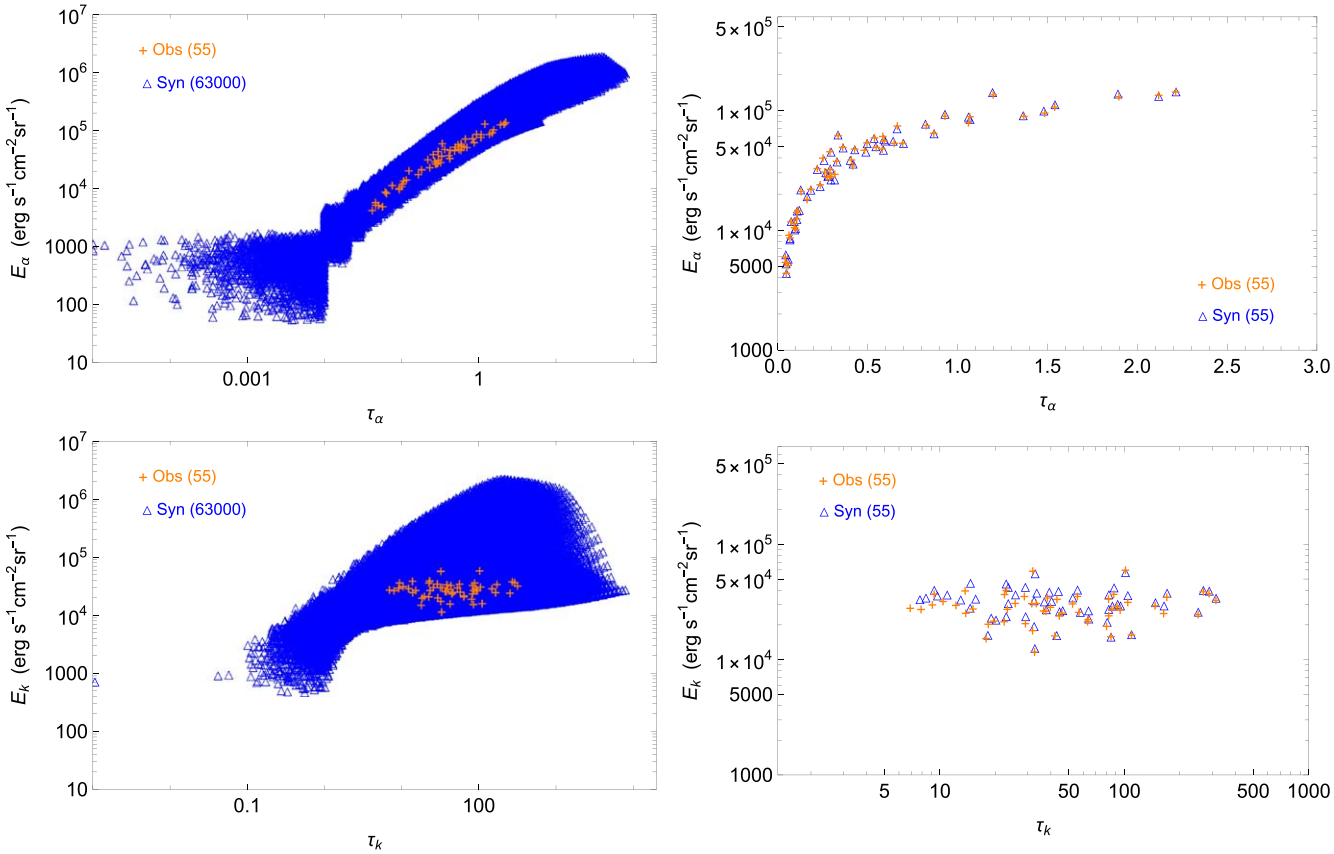

Figure 6. Integrated intensity emitted in the Hα line vs. the optical thickness of the Hα line for the observations and all synthetic models (upper left panel) and the same plot in the observational domain (upper right panel). The same plots are shown for the Mg II k line in the lower panels. The correlation coefficients in the right panels are shown in Table 2.

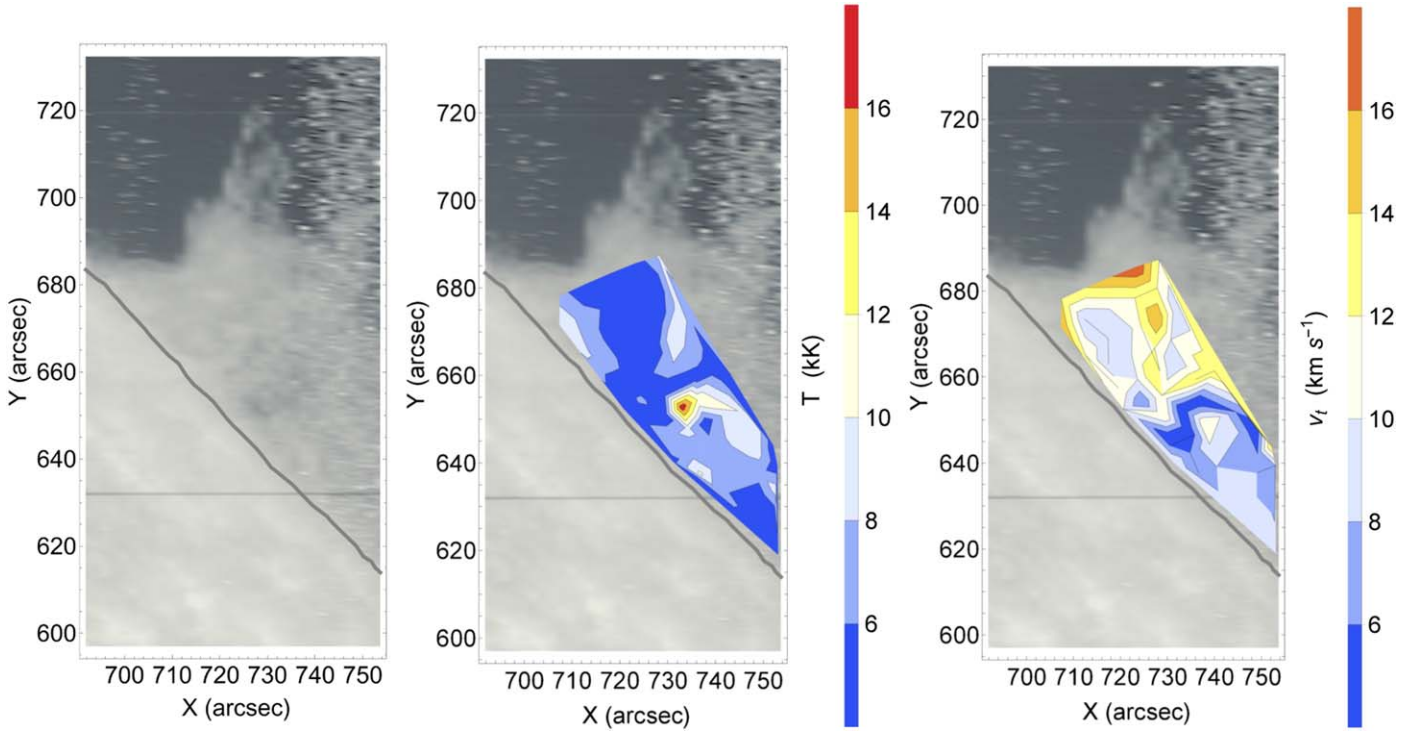

Figure 7. Intensity map of the studied prominence in IRIS 2796 SJ image with marked solar limb (left panel), distribution of kinetic temperature (middle panel), and microturbulent velocity (right panel).

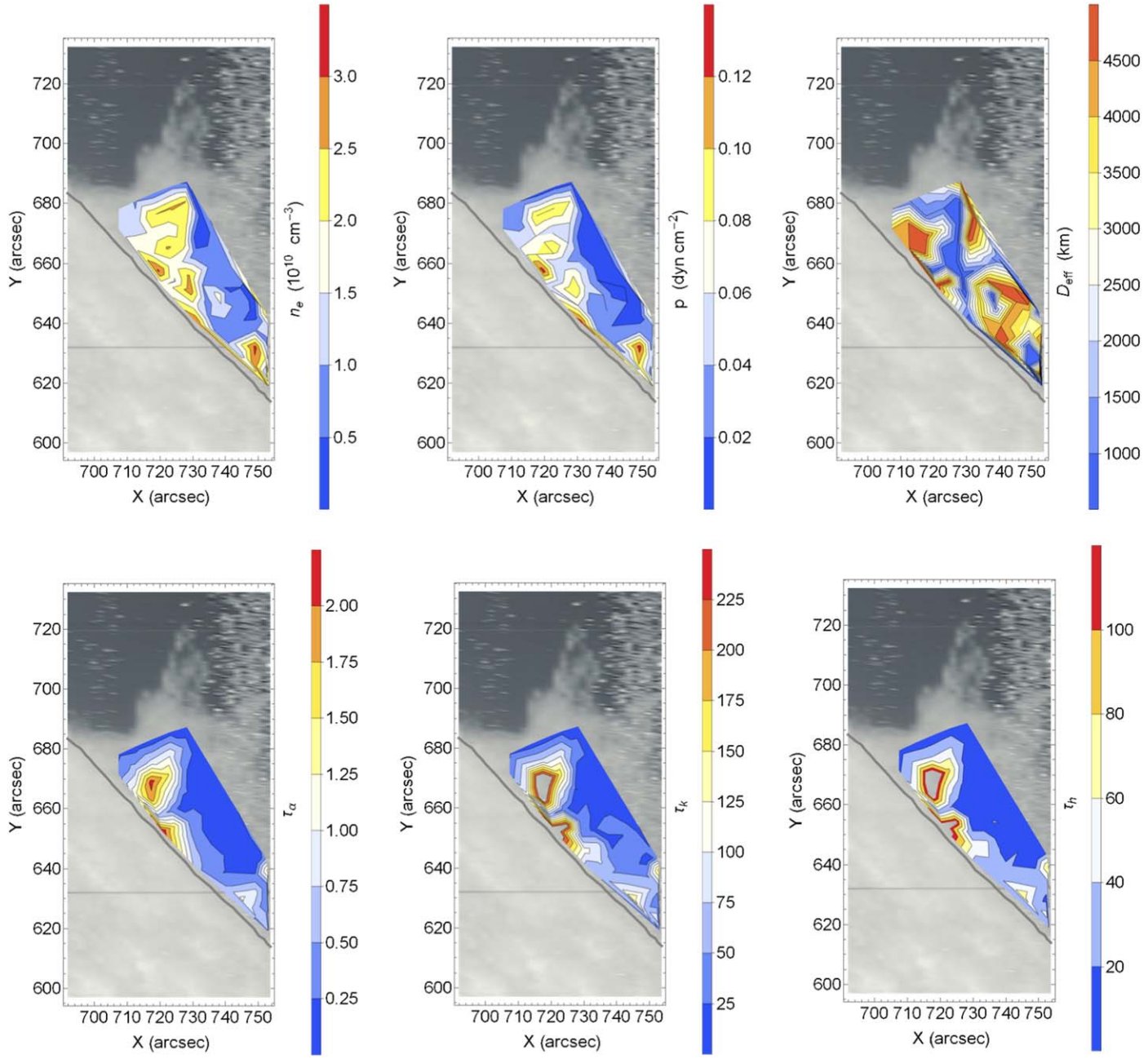

Figure 8. From left to right in the upper row: distribution of electron density, gas pressure, and effective thickness. From left to right in the lower row: distribution of optical thickness of the Hα line and both Mg II lines. For the original structure of the prominence in the IRIS 2796 SJ image see the left panel in Figure 7.

equilibrium are rather short, of the order of minutes, contrary to previous considerations (work in progress). However, the RE models of Heinzel et al. (2014) for low pressures and smaller thicknesses (see Table 2 therein) have generally higher temperatures. This then means that pixels with temperatures up to 10,000 K can also be in RE, contrary to the discussion in Okada et al. (2020). Models with very low temperatures below 5000 K may, however, have the following difficulty. In finding the RE models and also inverting the Mg II h&k lines we have so far used the simplified ionic model Mg II–Mg III, i.e., we neglected the population of Mg I ion. This is quite reasonable for typical chromospheric or prominence temperatures, but at low temperatures between 4000 and 5000 K, the Mg I ion can be significantly populated (M. Carlsson, private communication). Therefore, we have to be cautious in interpreting such low prominence temperatures, and further modeling is needed considering the complex system Mg I–Mg II–Mg III. At temperatures higher than say 20,000–30,000 K, the magnesium becomes fully ionized (see also Heinzel et al. 2014). For a general discussion of the prominence energy balance see Gilbert (2015).

Because our 1D-slab code represents only one uniform structure (like the whole prominence, its cool central parts) without any macroscopic dynamics, the only way to non-thermally broaden the line profiles is to increase the microturbulent velocity. This approach was also used for modeling the off-limb spicular forest, see Alissandrakis et al. (2018). However, the microturbulent and thermal broadening of the line profiles are closely coupled, both entering a single quantity, which is the Doppler width of the line. For optically

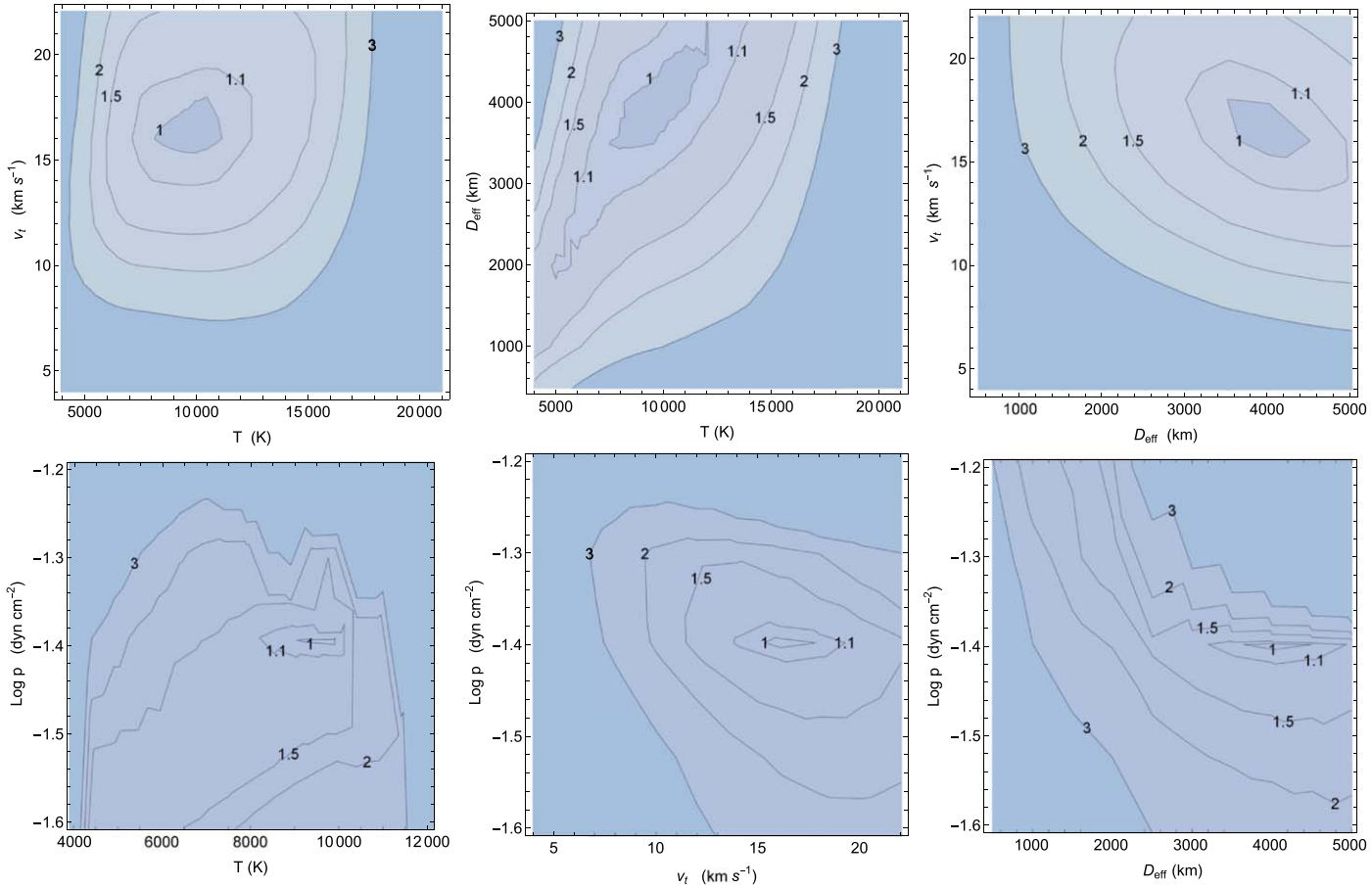

Figure 9. Contour plot of the merit function $\mathcal{L}$ in a 2D space shows in upper row from left to right: microturbulent velocity vs. kinetic temperature, effective thickness vs. kinetic temperature, and microturbulent velocity vs. effective thickness. The same plot for the lower row from left to right: gas pressure vs. kinetic temperature, gas pressure vs. microturbulent velocity, and gas pressure vs. effective thickness. All plots are made for one observed point within the prominence. Note that we plot the logarithm of the gas pressure since we use a logarithmic step in the non-LTE modeling.

thin lines with Gaussian line cores, the Doppler width directly relates to the FWHM. Therefore, if we increase microturbulent velocity, then the kinetic temperature should decrease in order to fit the observed FWHM. This can also be one of the reasons why we obtain low temperatures below 5000 K. This problem cannot be solved within the current modeling approach, but we made the following simple numerical experiment. Preliminary simulations of the Mg II line formation in multithread prominences with a stochastic distribution of line-of-sight velocities (Gunár et al. 2022) show that such structures produce a Mg II line FWHM that is significantly larger than for single-thread models without dynamics. The same applies also to the Hα line, see (Gunár et al. 2012). To account for such dynamical broadening of synthetic profiles, we therefore artificially enhanced the synthetic FWHM of both the Hα and Mg II k lines by a factor up to 1.5. As a result of the inversion, we obtained generally lower microturbulent velocities (lower than 12 km s^{-1}) and somewhat higher temperatures, compared to the scatter plot in the upper left panel of Figure 5. Namely, the lowest temperatures below 5000 K were much less populated. This is an expected trend that shows the importance of macroscopic dynamics for inversions.

We also tried an eight-parameter spectral inversion by adding the central intensities of the Hα and Mg II k lines, as well as the mean peak intensity of the Mg II k line (the mean between the blue and red peaks of the asymmetrical observed profiles). The Hα line-center intensity is in fact not an additional strong constraint because as can be seen from Figure 8 the majority of pixels have a line-center optical thickness below 1 and then, for a roughly Gaussian emission profile, the central intensity is a function of the integrated intensity and FWHM. However, the situation is completely different with the optically thick Mg II lines (see also Figure 8). The intensity in the line center and possibly in the peaks may reflect the presence of the PCTR (Heinzel et al. 2014), which is not included in present isothermal and isobaric models. Therefore, an eight-parameter inversion based on a grid of isothermal and isobaric models is in fact not applicable to the observed Mg II line profiles. 1D-slab models with PCTR have been proposed in, e.g., Anzer & Heinzel (1999) and recently used by Peat et al. (2021) to invert Mg II lines in another prominence. However, the latter authors did not attempt inverting Mg II lines together with the Hα line.

Here some comments are needed regarding the correlations shown in Figure 5. Contrary to theoretical correlations demonstrated in Jejčič et al. (2018, Figure 19), our ratio of Mg II k–Mg II h line intensities versus temperature shows a scattered cloud of points with no clear trend of increase with T. Such trend is visible in theoretical correlations of Jejčič et al. (2018), but the vertical range of the ratios due to variety of different models is rather large and this may result in the scatter visible in Figure 5, lower right panel. It is also possible that current observational data used for the inversion, and namely, low-resolution Hα, do not constrain well the temperature,

although adding the Mg II line ratio in our inversion improved the results, namely, the relation between temperature and microturbulent velocity. It is very difficult to assess the reasons for such behavior and as we conclude in the next section, new high-resolution data are urgently needed for more reliable inversions.

6. Conclusions

This paper is a continuation of Paper II in which we studied the same prominence observed simultaneously with the MSDP and IRIS spectrographs. MSDP provided data in the hydrogen Hα line, while for IRIS we selected both Mg II h&k lines. In Paper II, a spectral inversion was performed with only two Hα parameters, namely, the integrated intensity emitted in the Hα line and FWHM. As a result, two bifurcated solutions were found for the studied prominence: low kinetic temperature with a high microturbulence or high kinetic temperature and low microturbulent velocity. To test which state is more likely, in this work we performed a 1.5D spectral inversion where we added both magnesium lines. This is the first attempt to invert simultaneously Hα and Mg II h&k lines, which are generally optically thick and thus require complex non-LTE radiative transfer modeling.

To compare with observations, we first improved the integrated intensity emitted in the Hα line by extrapolating the narrow-band MSDP profiles. We also calculated the FWHM of the observed Hα line. The FWHM of the Mg II lines was based on their central intensities, an optional definition used consistently also for synthetic profiles. In the next step, we run a large grid of isothermal and isobaric 1D-slab models. The input parameters of the MALI code are kinetic temperature, microturbulent velocity, gas pressure, effective thickness, and height above the solar surface. We have assumed typical values for the input parameters of central cool parts of quiescent prominence (Table 1). In total, we computed 63,000 models. Obtained synthetic profiles were then convolved with the instrumental profile of both instruments to compare with the observations. Note that the convolution of the synthetic profiles with the instrumental profile affects the FWHM, but not the integrated intensity emitted in a specific line. Then we compared, in 55 selected points, the synthetic parameters of the Hα and Mg II lines, using five different observables for all three lines: the integrated intensities emitted in the Hα and Mg II k lines, the FWHM of these lines, and the ratio between the two magnesium lines. The model with $\mathcal{L}$ closest to 1 was chosen as the best fit for the selected observed prominence point. This means that we were able to estimate the physical conditions within the central part of the prominence, at each selected point. Note that our inversions were done using the large grid of synthetic profiles computed for the viewing direction perpendicular to the prominence slab, i.e., for $\mu = 1$. We constructed also another equivalent grid for $\mu = 0.5$, but the results of inversion are similar.

The present spectral inversion leads to a solution with lower kinetic temperatures and a relatively low microturbulent velocity. The results are presented as scatter plots and 2D maps where the temperatures and microturbulent velocities are mostly in the range of values generally considered for quiescent prominences (Bendlin et al. 1988). Using only the Hα line led to a bifurcated solution (Paper II), while adding the coaligned Mg II data largely improves the solution. Our recent experience with a more complex 2D multithread dynamical modeling (each thread having its own PCTR and velocity) demonstrated substantial departures from simple 1D-slab modeling both for hydrogen Lyman lines (see, e.g., Gunár et al. 2008, 2010) and for Mg II lines (Gunár et al. 2022). The line inversions based on such complex modeling will be the subject of our future work. For that, we will also need new high-resolution, well-coaligned simultaneous observations in several lines of different species to make the inversions more reliable.

S.J. acknowledges the support from the Slovenian Research Agency No. P1-0188. P.H., S.G., and S.J. acknowledge support from grant No. 19-17102S of the Czech Funding Agency. S.G. and P.H. acknowledge support from grant 19-16890S of the Czech Funding Agency and from RVO:67985815 project of the Astronomical Institute of the Czech Academy of Sciences. P.H. was also supported by the project of the Wrocaw University No. BPIDUB.4610.96.2021.KG. B.S. is thankful for the financial support for a visit to Ondřejov Observatory. G. P.R. acknowledges the support by the NNSFC grant 12173022, U1831107. We thank the anonymous referee for his/her constructive comments and suggestions, which greatly improved the paper.

ORCID iDs

Sonja Jejčič https://orcid.org/0000-0001-8489-4037
Petr Heinzel https://orcid.org/0000-0002-5778-2600
Brigitte Schmieder https://orcid.org/0000-0003-3364-9183
Stanislav Gunár https://orcid.org/0000-0003-3889-2609
Guiping Ruan https://orcid.org/0000-0002-3232-0071

References

Alissandrakis, C. E., Vial, J. C., Koukras, A., Buchlin, E., & Chane-Yook, M. 2018, SoPh, 293, 20
Anzer, U., & Heinzel, P. 1999, A&A, 349, 974
Barczynski, K., Schmieder, B., Peat, A. W., et al. 2021, A&A, 653, A94
Beck, C., Gosain, S., & Kiessner, C. 2019, ApJ, 878, 60
Bendlin, C., Wiehr, E., & Stellmacher, G. 1988, A&A, 197, 274
da Silva Santos, J. M., de la Cruz Rodríguez, J., Leenaarts, J., et al. 2020, A&A, 634, A56
De Pontieu, B., Title, A. M., Lemen, J. R., et al. 2014, SoPh, 289, 2733
Gilbert, H. 2015, in Solar Prominences, Astrophysics and Space Science Library, Vol. 415, ed. J.-C. Vial & O. Engvold (Cham: Springer), 157
Gouttebroze, P. 2007, A&A, 465, 1041
Gunár, S., Heinzel, P., Anzer, U., & Schmieder, B. 2008, A&A, 490, 307
Gunár, S., Heinzel, P., Schwartz, P., & Koza, J. 2022, ApJL, submitted
Gunár, S., Koza, J., Schwartz, P., Heinzel, P., & Liu, W. 2021, ApJS, 255, 16
Gunár, S., Mein, P., Schmieder, B., Heinzel, P., & Mein, N. 2012, A&A, 543, A93
Gunár, S., Schwartz, P., Koza, J., & Heinzel, P. 2020, A&A, 644, A109
Gunár, S., Schwartz, P., Schmieder, B., Heinzel, P., & Anzer, U. 2010, A&A, 514, A43
Heasley, J. N., & Mihalas, D. 1976, ApJ, 205, 273
Heinzel, P., & Anzer, U. 2012, A&A, 539, A49
Heinzel, P., Susino, R., Jejčič, S., Bemporad, A., & Anzer, U. 2016, A&A, 589, A128
Heinzel, P., Vial, J. C., & Anzer, U. 2014, A&A, 564, A132
Jejčič, S., Schwartz, P., Heinzel, P., Zapiór, M., & Gunár, S. 2018, A&A, 618, A88
Koza, J., Gunár, S., Schwartz, P., Heinzel, P., & Liu, W. 2022, ApJ, submitted
Koza, J., Kuridze, D., Heinzel, P., et al. 2019, ApJ, 885, 154
Labrosse, N., Heinzel, P., Vial, J. C., et al. 2010, SSRv, 151, 243
Levens, P. J., & Labrosse, N. 2019, A&A, 625, A30
López Ariste, A. 2015, in Solar Prominences, Astrophysics and Space Science Library, Vol. 415, ed. J.-C. Vial & O. Engvold (Cham: Springer), 179
Machol, J., Snow, M., Woodraska, D., et al. 2019, E&SS, 6, 2263
Mackay, D. H., Schmieder, B., López Ariste, A., & Su, Y. 2020, A&A, 637, A3

Martínez González, M. J., Asensio Ramos, A., Arregui, I., et al. 2016, ApJ, 825, 119
Martínez González, M. J., Manso Sainz, R., Asensio Ramos, A., et al. 2015, ApJ, 802, 3
Mein, P. 1977, SoPh, 54, 45
Mein, P. 1991, A&A, 248, 669
Mein, P., & Mein, N. 1991, SoPh, 136, 317
Merenda, L., Trujillo Bueno, J., Landi Degl'Innocenti, E., & Collados, M. 2006, ApJ, 642, 554
Molowny-Horas, R., Heinzel, P., Mein, P., & Mein, N. 1999, A&A, 345, 618
Okada, S., Ichimoto, K., Machida, A., et al. 2020, PASJ, 72, 71
Peat, A. W., Labrosse, N., Schmieder, B., & Barczynski, K. 2021, A&A, 653, A5
Riethmüller, T. L., Solanki, S. K., Barthol, P., et al. 2017, ApJS, 229, 16
Ruan, G., Jejčič, S., Schmieder, B., et al. 2019, ApJ, 886, 134
Ruan, G., Schmieder, B., Mein, P., et al. 2018, ApJ, 865, 123
Sainz Dalda, A., de la Cruz Rodríguez, J., De Pontieu, B., & Gošić, M. 2019, ApJL, 875, L18
Snow, M., Weber, M., Machol, J., Viereck, R., & Richard, E. 2014, JSWSC, 4, A04
Tziotziou, K., Heinzel, P., Mein, P., & Mein, N. 2001, A&A, 366, 686
Vial, J.-C., & Engvold, O. 2015, Solar Prominences: Astrophysics and Space Science Library, Vol. 415 (Cham: Springer)
Wang, S., Jenkins, J. M., Martinez Pillet, V., et al. 2020, ApJ, 892, 75
Warren, H. P., Mariska, J. T., & Wilhelm, K. 1998, ApJS, 119, 105